(article starts on next page)

Interactions between Automotive Shredder Residue and Olivine Bed Material during Indirect Fluidized Bed Gasification

Robin Faust,* Panida Aonsamang, Jelena Maric, Alyona Tormachen, Martin Seemann, and Pavleta Knutsson

ACCESS | 📊 Metrics & More | 📑 Article Recommendations

ABSTRACT: Thermal conversion of automotive shredder residue (ASR) using indirect fluidized bed gasification was conducted in the Chalmers semi-industrial 2−4-MW$_{th}$ gasifier. The bed material consisted of olivine that was activated through the deposition of biomass ash prior to a 13-day exposure to ASR. The interactions between the bed material and the ASR ash were investigated using XRD, SEM-EDS, and thermodynamic modeling. The deposition of iron (Fe) onto the olivine particles was noted, and this is likely to increase the oxygen-carrying ability of the particles. Furthermore, at the end of the campaign, about one-third of the particles in the bed were found to originate from the ASR ash. These particles were rich in Fe and Si, as well as elements found exclusively in the ASR ash, such as Zn, Ti, and Cu. Some of these particles exhibited a hollow morphology, suggesting a melt state during their formation in the gasifier. In addition, a low level of agglomeration of the ash and olivine particles was detected. Thermodynamic modeling with the FactSage software indicated the formation of slag. This study presents a detailed investigation of the interactions that occur between the bed material and an ash-rich fuel such as ASR. The findings may have applications in demonstrating the induction of oxygen-carrying ability in bed materials or for metal recycling through the separation of ash particles from the bed material.
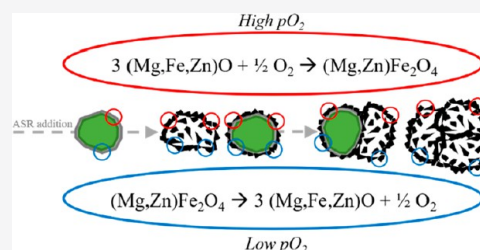
1. INTRODUCTION

Approximately 10 million end-of-life vehicles (ELVs) are generated annually in the European Union (EU). About two-thirds of these vehicles are treated according to the EU ELV Directive (2000/53/EC).[1] The EU ELV Directive states that the rate of reuse and recovery of ELVs must be 95% (per vehicle and year) and that the rate of reuse and recycling must be 85%.[2] After depollution and dismantling of spare parts, ELVs are commonly shredded to allow recovery of their metal content.[1,3,4] The fraction that remains after the primary recovery processes is called automotive shredder residue (ASR), which accounts for around 25% of the ELV.[5]

ASR is a heterogeneous fraction that consists of different materials, such as plastic, metal, rubber, foam, and glass.[6] The composition of the ASR fraction depends on the materials that are fed into the shredder, the effectiveness of the shredder, the separation processes, and the postshredder techniques.[5,7−10] The heterogeneity of ASR is further exacerbated by the differences in ELV models, as, for example, the newer types of ELVs contain higher levels of plastics and electronics than the older models.[11,12] In the EU, ELVs are commonly treated and sorted by authorized treatment facilities according to the legislation.[13] Furthermore, numerous postshredder separation technologies are available (e.g., air classification, magnetic and eddy current separation, wet treatment, hydrocyclone, etc.), whereas in some practices, ELVs are exported to lower-income

countries for manual sorting.[10] Due to the challenges associated with its complexity, a large fraction of the ASR is commonly landfilled.[14−17] However, due to the presence of hazardous compounds, such as chlorine, contaminated oil, and heavy metals, in ASR,[5,10] the EU only allows 5% of the ELV to be disposed of in landfills.[18] The restrictions on landfilling ELVs mean that there is a need for more extensive treatment of the ASR material flows so that the waste streams can be decreased.

Different methods for energy recovery from ASR have been investigated in the literature, including incineration, pyrolysis, and gasification.[7,10,19−21] The outcomes of the performed studies reveal that thermal conversion of ASR is associated with various environmental and technical issues.[10] One of the major environmental concerns is that polychlorinated dibenzo-*p*-dioxins (PCDDs) and dibenzofurans (PCDFs) can form during incineration, and they need to be controlled and treated before the exhaust gases are released into the environment.[21−23] Currently, dioxin- and furan-containing compounds are treated using calcium-based filters and activated carbon, which results in
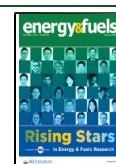
higher operational costs.[10,21,24] The costs associated with gas treatment can be reduced by inhibiting the formation of dioxins, which can be achieved by varying the amount of oxygen present during combustion, decreasing the presence of species that catalyze dioxin formation, and adjusting the reactor temperature and residence time of the gas during the thermal conversion process.[21] Decreasing the concentration of oxygen in the system during thermal conversion has been observed to significantly lower the levels of dioxins, which is why indirect gasification of ASR is considered to be a relevant technique for the thermal conversion of ASR.[21,23]

Indirect gasification is a thermal conversion technique that separates the exothermic combustion reaction from the endothermic gasification reaction by employing two separate reactors (see Figure 1), wherein the heat required for the
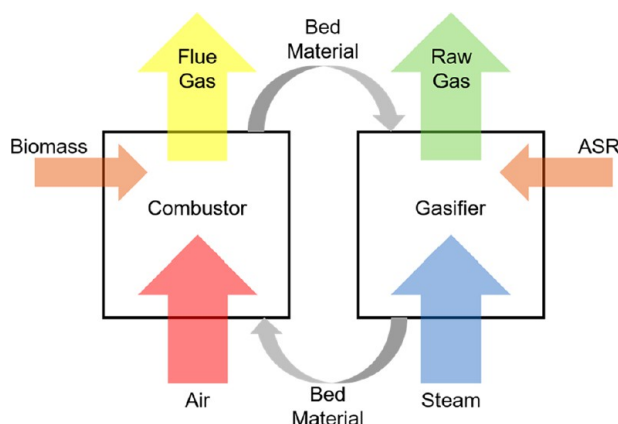

Figure 1. Schematic representation of the indirect dual fluidized bed (DFB) setup used for the gasification of automotive shredder residue (ASR).

endothermic gasification reaction is provided by a circulating fluidized bed material in a dual fluidized bed (DFB) system. The bed material in the fluidized bed further increases the contacts between the fuel particles and the surrounding gas, thereby enabling the conversion of lower-grade fuels, such as the ASR fraction. The inorganic ash fraction of the fuel remains within the system and interacts with the bed material, such that it can change the properties of the bed. Interactions of fuel ash and bed material have been extensively studied for biogenic fuels.[25−34] Depending on the choice of bed material, agglomeration can occur when quartz sand (SiO_2) is applied. However, in studies using olivine $[(Mg, Fe)SiO_4]$ or feldspar $[(K, Na)AlSi_3O_8]$ the formation of an ash layer was reported which exhibits catalytic activity toward tar reduction in the raw gas. Furthermore, Berdugo Vilches et al.[35] found that longer residence times can invoke the oxygen-carrying ability of originally inactive material. This led to a decrease in H_2 in the raw gas, decreasing the overall calorific value of the product.

In the case of the Chalmers gasifier, the combustor is fed with biomass as the fuel, while air is used as the fluidization gas. The gasifier side is fluidized with steam, and ASR is utilized as the fuel. Thus, a low oxygen partial pressure is realized in the reactor in which the ASR is converted, which decreases the generation of dioxins. Furthermore, decomposition of the ASR into monomer-like compounds (such as ethylene and styrene) occurs during DFB gasification, which makes the product gas valuable for the petrochemical industry.[36] After fuel conversion, the formed ASR ash, which is rich in transition metals, increases

in concentration throughout the process. Thus, continuously feeding and converting ASR increases the concentrations of transition metals in the bed material, and these metals can act as oxygen carriers so as to increase the oxygen-carrying ability of the bed. If the oxygen-carrying ability of the bed material employed in the DFB process is considerable, as is the case with particles with high contents of transitions metal oxides, the process turns into a chemical looping gasification (CLG).

Pissot et al.[7] studied the thermochemical recycling of ASR using CLG. Based on the results of the CLG experiments, Fe was identified as one of the main constituents of the ash and was considered most likely to be the main oxygen-carrying compound in the bed. Other compounds that were identified as having minor contributions to the oxygen transport were Ni, Mn, and Cu. The study of Pissot et al.[7] also showed that the presence of S in the ash could further add to the oxygen carrying through cycles of $CaSO_4/CaS$, as described earlier.[37] Thus, that study[7] confirmed the beneficial effects of the inherent oxygen carriers accrued from the ASR ash interaction with the bed material under CLG conditions. The oxygen-carrying ability of the bed material was also designated as the parameter of highest importance for achieving efficient char conversion. However, as oxygen carriage decreases the calorific value of the raw gas by converting H_2 and CO to H_2O and CO_2, respectively, this is a major trade-off for CLG.

To obtain a product gas with high calorific value while at the same time maintaining a high degree of char conversion, it is necessary to establish an equilibrium between the oxygen-carrying properties of the formed ASR ash. Previous studies of DFB gasifiers have pointed out the importance of the fuel ash chemistry for process optimization. Understanding the reactions between the ash and bed material is, therefore, crucial for the outcome of the process. As ASR is a particularly ash-rich fuel, the used bed material is expected to be rich in metals that originate from the ASR, and these metals could potentially be recycled from the spent bed material.

The material for this study originates from a CLG experiment by Pissot et al.[7] where the focus has been on product gas optimization. Partial analysis of the material has previously been conducted by Staničić et al.[38] with the main focus on trace elements. In the present study, the focus has been on the morphology and changes in chemical composition of the bed material as a result of the interaction with ASR ash. The aim is to elucidate the challenges and possibilities for the bed material, related to the application of ASR as a fuel in comparison to biomass for DFB gasification. Results of this study can indicate whether the bed material forms similar catalytic layers as observed with biomass which allows the utilization of ASR as a possible future feedstock.

2. EXPERIMENTAL SECTION

2.1. Materials and Experimental Campaign. The bed material samples used in this study were obtained in a 2-week-long experimental campaign carried out in the Chalmers indirect gasifier at Chalmers University of Technology. The research unit is composed of a bubbling fluidized bed gasifier ($2−4$-MW_{th}) integrated with a $10−12$-MW_{th} circulating fluidized bed (CFB) boiler. More details about the research unit can be found elsewhere.[39] The fluidization media used were steam in the gasifier and air in the boiler. The gasifier was operated during daytime for the purpose of the research, while the boiler is usually running continuously, producing heat for the campus. The boiler used approximately 1500 kg/h of wood chips with about 0.7 wt % ash. As the bed material, olivine sand with the composition presented in Table 1 was used. The total bed inventory in the system was about 4 tonnes.

Table 1. Chemical Composition of the Olivine Particles Used as Bed Material in the Present Study[a]

	wt %
MgO	49.6
SiO_2	41.7
Fe_2O_3	7.40
Al_2O_3	0.46
Cr_2O_3	0.31
NiO	0.32

[a]The values shown are in weight percent (wt %).

The ASR, which was provided by Stena Recycling AB and contained about 47 wt % ash (see Table 2), was fed into the gasifier at a rate of 270

Table 2. Ash Fractions (Dry Fuel Basis) and Feeding Rates of the Two Fuels (as Received) Used in This Study

	ASR	wood chips
ash fraction (wt %)	47	0.7
feeding rate (kg/h)	270−300	1500−2000

kg/h. The compositions of the ash fractions of both the wood chips and ASR are listed in Table 3. The main ash elements found in wood chips are Ca, K, and Mg, whereas ASR ash is most abundant in Si, Fe, and Al.

Table 3. Compositions of the Two Ash Fractions, Presented in Atomic Percent (at. %)

	ASR	wood chips
Na	4.4	1.9
Mg	3.7	10.7
Al	11.8	1.2
Si	31.1	4.3
P	0.6	2.8
S	1.4	6.8
Cl	1.9	3.1
K	1.4	26.4
Ca	9.6	40.7
Ti	1.2	0.2
Cr	0.2	0
Mn	0.3	1.4
Fe	26.1	0.4
Ni	0.1	0
Cu	1.1	0
Zn	4.5	0
Ba	0.5	0.2
Pb	0.1	0

The focus of the present experiment was on the influence of ash enrichment of the bed. In order to collect representative bed samples, the removal and eventual addition of the bed inventory were done only to the extent that a stable pressure was maintained in the boiler. The experimental campaign, which was started with fresh olivine as the bed material and wood chips as the fuel, ran for 1 week in CFB mode. Thereafter, ASR was fed as fuel into the system on the gasifier side. Bed samples were extracted from the reactor at four different time points after the start of ASR addition: day 1, day 4, day 7, and day 13. A schematic overview of the exposure history and sampling schedule is shown in Figure 2.

2.2. Material Preparation and Analysis. Scanning electron microscopy (SEM; FEI ESEM Quanta 200) was conducted on cross sections of the samples, which were prepared using two different methods: (1) epoxy embedding and subsequent grinding and polishing with SiC paper, for overview scans and statistical analysis, and (2) broad ion beam (BIB; Leica EM TIC 3X) milling, whereby a low number of particles was fixated with glue between two silicon wafers and subsequently milled, to achieve better surface quality of the particle cross section, in order to enhance the imaging resolution.

The contrast generated from backscattered electrons (BSE) was utilized for particle differentiation, and the acceleration voltage was usually set to 15 kV.

X-ray diffraction (XRD; Siemens D8) was performed to study the formed crystallographic phases. Cu−K_α radiation was used, and the scan was recorded for 2θ in the range of 10°−90°. The samples were ground prior to the analysis. To study the impact of reducing conditions on the crystallographic composition, one sample was exposed for 40 s to a mixture of 50% CO and 50% N_2 in a batch reactor at 850 °C and analyzed with XRD. Additional information on the reactor design can be found elsewhere.[40]

2.3. Thermodynamic Modeling. The FactSage 7.2 software[41] was utilized for the thermodynamic modeling, using the FactPS, FToxid, and FTsalt databases. The equilibrium calculations were conducted at 850 °C and at a pressure of 1 atm.

Thermodynamic modeling was used to investigate the phase transformations that the ash particles underwent when they were cycled between oxidizing and reducing conditions. The oxygen partial pressure for the oxidizing condition in the boiler was assumed to be 0.2 atm. In the gasifier, the partial pressure of oxygen was calculated to be on the order of magnitude of 1×10^{-18} atm, given the composition of permanent gases leaving the gasifier, as reported by Pissot et al.,[7] where the gas composition of the same experiment was investigated.

3. RESULTS AND DISCUSSION

SEM micrographs of cross sections, prepared by epoxy embedding and grinding with SiC paper, of all four olivine samples are shown in Figure 3. The olivine particles were exposed for 7 days to wood chips prior to the experimental campaign with ASR (see Figure 2). Therefore, the ash layer formation characteristic of the interaction of olivine with biomass ash can be seen already in the day 1 sample.[26,31,42−44]
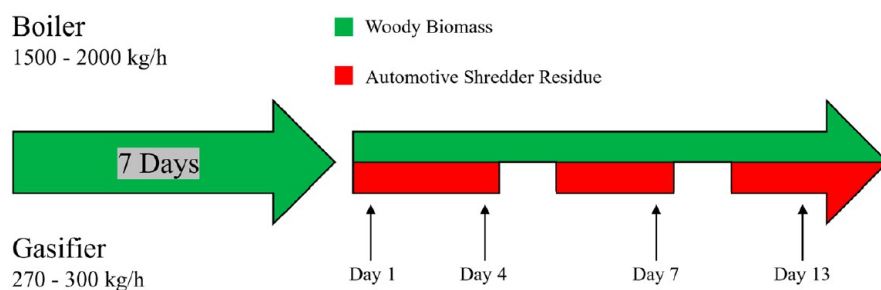

Figure 2. Schematic overview of the exposure history of the samples investigated in this study. Before the start of the addition of ASR to the gasifier, the particles were exposed to woody biomass for 7 days. The gasifier was fed with ASR for about 6 h during the days of operation, which was interrupted during weekends. The boiler was fed with woody biomass throughout the entire exposure period.
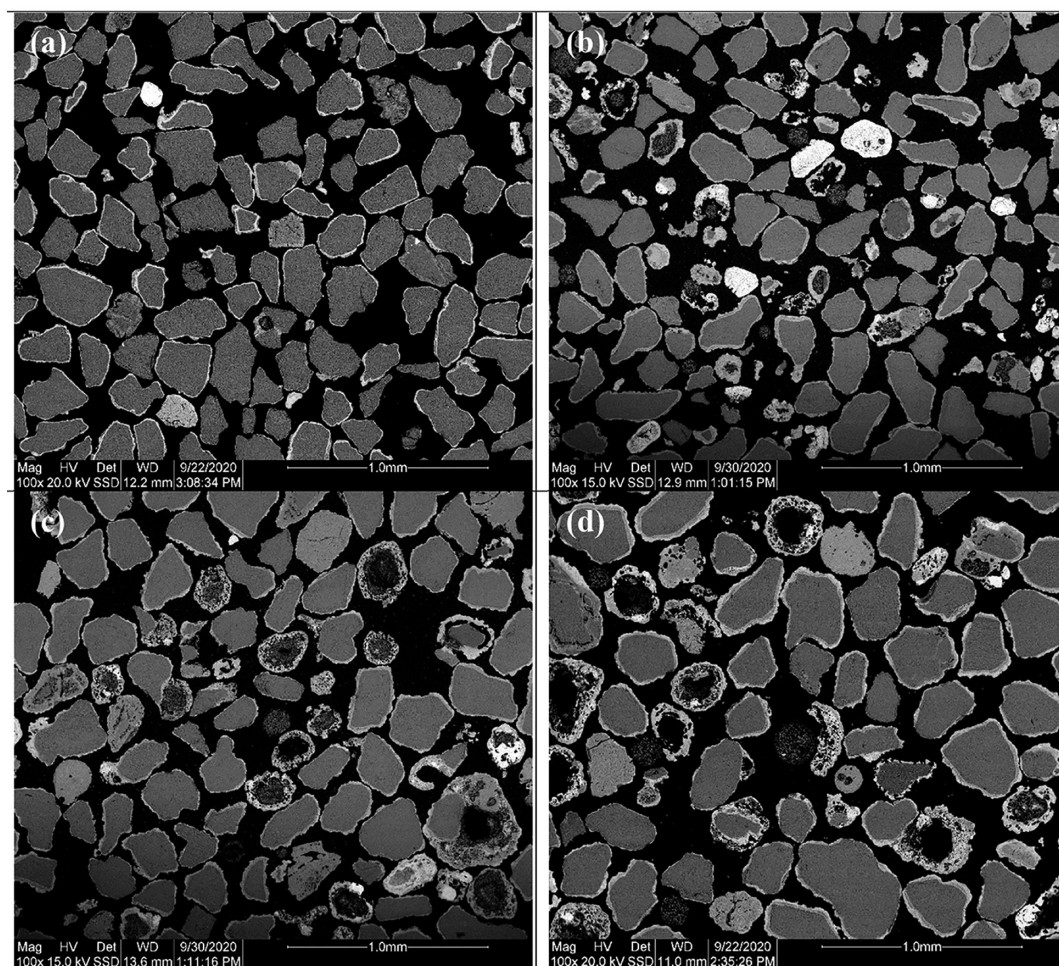
Figure 3. SEM cross-sectional overview micrographs of bed material samples extracted on day 1 (a), day 4 (b), day 7 (c), and day 13 (d) of the experimental campaign.

Throughout the period of exposure to ASR, an ash layer that is steadily increasing in thickness forms around the particles. On day 13, all of the particles are surrounded by a thick ash layer, which appears bright in BSE contrast.

It can also be seen in Figure 3 that several particles appear brighter and do not exhibit the typical surrounding layer structure. The difference in BSE contrast is due to the different chemical compositions of the particles, whereby a higher average atomic number (than olivine) gives the appearance of a brighter contrast. The particles that originate from the ASR ash consist mainly of Fe. As Fe has a higher average atomic number than olivine, it may be responsible for the observed brighter contrast. EDS-point analysis confirmed the presence of a high concentration of Fe in the brighter particles. These particles can already be observed after 1 day (Figure 3a) and to a higher amount after 4, 7, and 13 days (Figure 3b–d). The relative amount of these particles is significant, which is why they are discussed separately in section 3.2.

3.1. Layer Formation on Olivine Particles. At the start of the experiment, the bed material particles were in an "active state". "Active" in this case refers to the catalytic activity toward tar cracking during gasification which the particles exhibit due to the deposition of ash elements from biomass. The activation of the particle occurred through exposure of the particles to biomass as the fuel for 1 week. As a consequence, the particles

exhibited a surface layer that was rich in biomass ash-derived elements shortly after the ASR was introduced (see Figure 3a).

To characterize the influence of the introduced ASR on ash layer development, further analyses were performed on the samples collected on day 1 and day 13 after introduction of the ASR fraction into the gasifier. Micrographs of the cross sections of two representative particles are shown in Figure 4. In the micrographs, it can be seen that both particles are covered with an ash layer of varying thickness, with the ash layer being thicker in the particle that had a longer residence time. The formation of a homogeneous inner layer is well-established in the literature[31,42,45−47] and can be seen also in Figure 4b. After prolonged exposure to the ASR ash, the layer increases in porosity; this change can be followed in panels c and d of Figure 4.

EDS mapping was performed on the layer of the particle exposed for 13 days to the ASR (Figure 5). Similar to the previously published results on the interaction of olivine with biomass ash, the homogeneous inner layer is rich in Ca and Si.[31,42] However, in the previous studies, the outermost surface of the olivine particles that had been exposed to biomass ash only was found to be enriched for Mg but with a low concentration of Si.[42] A similar layer is observed in the present study, albeit in the center of the ash layer. Its location is indicated by the dashed line in Figure 5. Based on the location of this Mg-enriched layer, it can be speculated that the layer underneath the
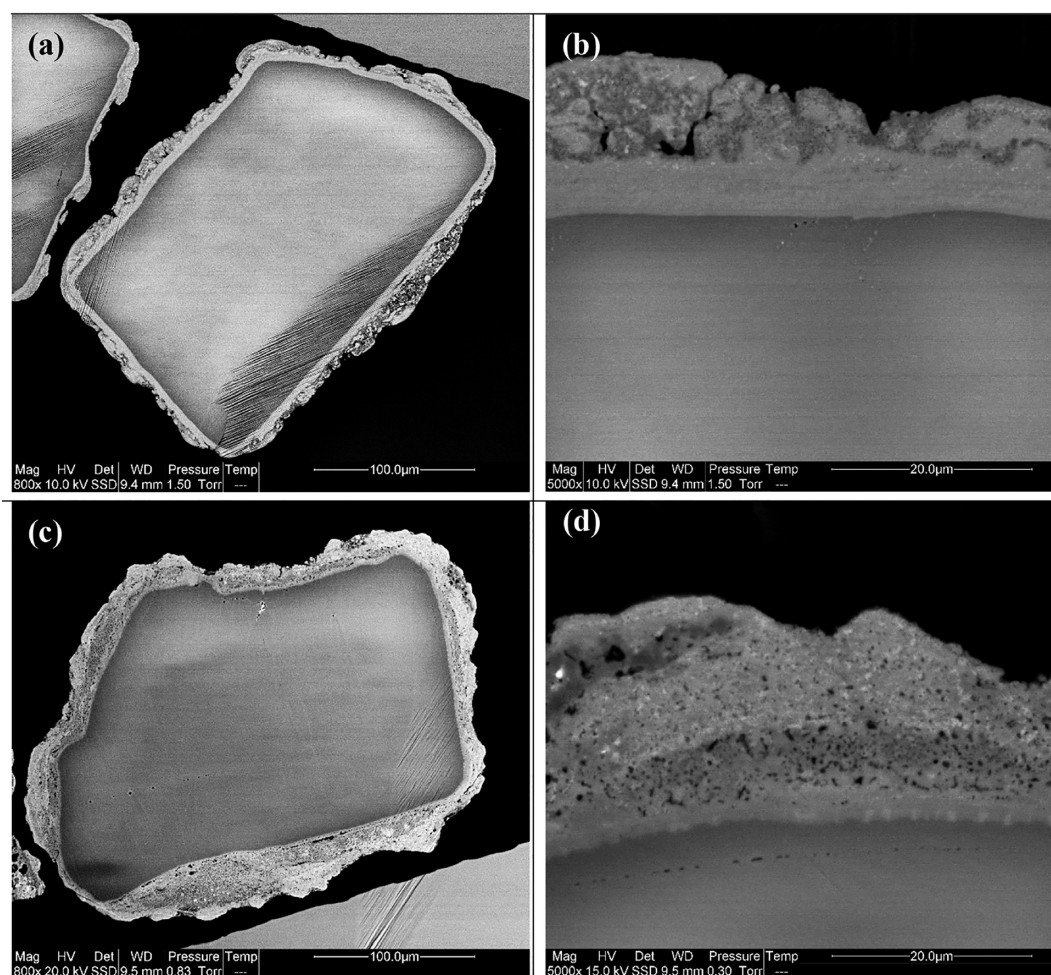
Figure 4. SEM micrographs of the cross sections prepared with broad ion beam milling of representative olivine particles extracted after 1 day (a)−(b) and 13 days (c)−(d) of exposure to ASR.

line formed during the 7 days of the activation process with woody biomass, prior to the experimental campaign with ASR. This indicates that the layer above the dashed line formed due to interactions with the ASR ash. Indeed, the concentrations of elements such as Na, Al, Ti, and Fe detected in the ASR ash (with only minor amounts in biomass ash) are higher above the dashed line than underneath the dashed line.

An EDS line scan recorded at the same location as the intensity maps is shown in Figure 6, in which the aforementioned formation of two layers is indicated. The composition of the outermost layer, which formed due to ASR ash interactions, contains around 20 at. % Fe, as compared to 5 at. % Fe in the area underneath this layer. The reported increase in the oxygen-carrying ability of the bed material[36] is most likely attributable to the higher Fe concentration in the outermost layer. For comparison, previous studies on the interaction of olivine with biomass ash have reported the presence of around 10 at. % Fe on the particle surface, which means that there is twice as much Fe in the outermost layer when ASR is used as the fuel.[26,42,44,48] The Fe localized to the outermost layer is, therefore, expected to originate from the ASR ash.

Thermodynamic calculations were conducted based on the elemental composition of the bed material extracted after 13 days of feeding ASR into the gasifier (see Table 4). The oxygen partial pressures typical for oxidizing and reducing conditions were assumed to be 0.2 and 1×10^{-18} atm, respectively. The

pressure level of 0.2 atm corresponds to the air present in the combustor, and the 1×10^{-18} atm relates to the composition of the raw gas reported by Pissot et al.,[7] where on day 13, the CO/CO$_2$ ratio was around 1 and the temperature was 820 °C. The results of the calculations are shown in Figure 7. Alternating between oxidizing and reducing conditions affects the oxidation state of Fe. From the performed thermodynamic calculations, it is clear that Fe-rich olivine and Fe-rich metal oxide, (Fe, Mg, Zn)O, form under reducing conditions, in contrast to spinel (Mg,Zn)Fe$_2$O$_4$, which forms under oxidizing conditions. The formation of ZnFe$_2$O$_4$ was confirmed by the group of Staničić in a study that involved the same material as that used in the current work.[38,49] Previous publications on biomass ash-coated olivine have described lower concentrations of Fe, which explains why the thermodynamic equilibrium calculations conducted in the previous studies did not result in spinel formation under oxidizing conditions.[26,42,43] Therefore, the particles are expected to have significantly higher oxygen-carrying capabilities when an iron-rich fuel is utilized.

When interpreting the results from these calculations, it should be noted that the presented results are calculated at the equilibrium state and for stagnant conditions, with the assumption that the entire olivine particle experiences the alternating conditions. In a real-life scenario, the particles are constantly circulating between the combustor and gasifier, which makes it unlikely that they would reach equilibrium.
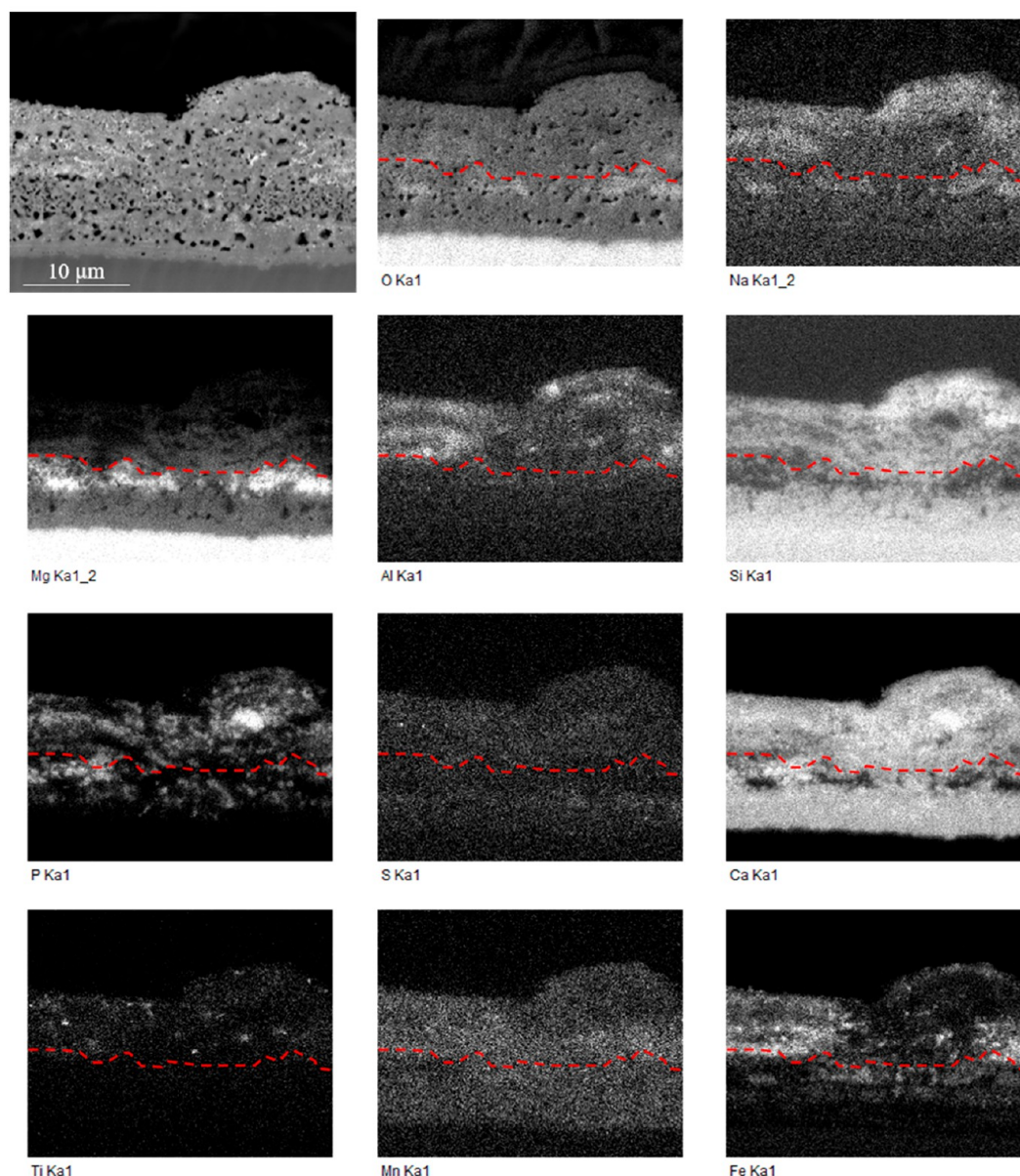
Figure 5. BSE micrograph and EDS mappings recorded on a cross section of a particle extracted on day 13 of the experimental campaign. The red line indicates the interface between the ash layer derived from biomass ash elements and the ash layer formed as a result of interaction with the ASR ash.

Nevertheless, the changes shown in Figure 7 are still expected to occur on the surfaces of the particles.

To evaluate the applicability of the thermodynamic calculations, the changes in phase composition depicted in Figure 7 for reducing conditions and for the olivine samples were tested experimentally. This was achieved by reducing the sample extracted after 13 days for 40 s in a batch reactor in an atmosphere that consisted of 50% CO with 50% N_2. XRD was conducted on the sample both before and after exposure to the reducing conditions, in order to characterize the change in phase composition before and after the experiment. The results are shown in Figure 8. After exposure to the reducing atmosphere, the most prominent change is a reduction in the intensity of the peak at $2\theta = 35.4°$, which corresponds to a peak for magnetite (Fe_3O_4). Fe is expected to change the degree of oxidation from 3^+ to 2^+ when subjected to reducing conditions, which explains the decrease in intensity of the peak corresponding to magnetite. Additional noteworthy changes are observed as decreases in the

peaks for the mixed oxides $CaMgSi_2O_6$ and $Ca_2ZnSi_2O_7$. These phases are expected to form only under oxidizing conditions and disappear when reducing conditions are applied (Figure 7). This is because Ca, Mg, and Zn can be incorporated into the olivine solid solution, and olivine is more abundant under reducing conditions, which means that it can dissolve higher levels of these elements.

Comparing the results of the thermodynamic calculations with the results obtained from XRD, it is evident that the assumed equilibrium state is unlikely to be reached within the applied period of exposure. This is not unexpected, as only atoms in the vicinity of the surface are able to participate in reactions with the gas phase. However, the trend seen in the XRD is the same as that derived from the thermodynamic equilibrium calculations, where the most significant change between the reduced and oxidized phases is the reduction in phases that contain Fe^{3+} when reducing conditions are applied.
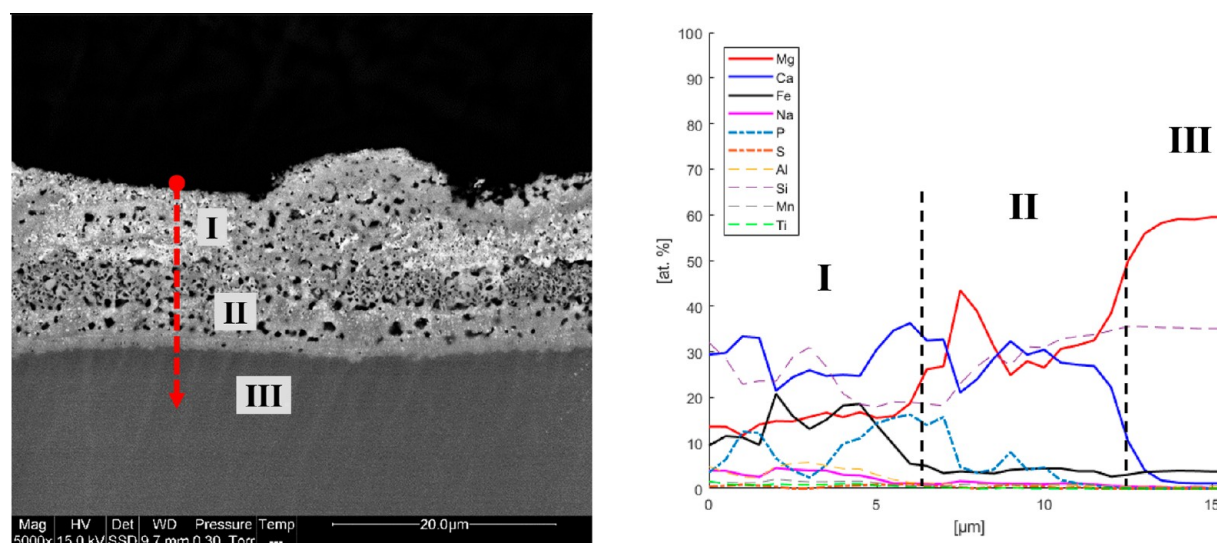
Figure 6. BSE micrograph (left) and EDS line scan (right) (O- and C-free basis) of the ash layer formed on a particle extracted after 13 days of exposure to ASR. The indicated areas (I–III) refer to the layers formed due to interaction with the ASR ash (I), interaction with the biomass ash (II), and the unreacted olivine (III).

Table 4. Composition (in Atomic Percent) of the Bed Material after 13 Days of Feeding ASR into the Gasifier (O-Free Basis)[a]

Mg	Si	Ca	Fe	Al	K	Na	P	Zn	Mn	Ti	Cu	S	Ni	Ba	Cr
38.9	33.7	9.3	7.2	3.1	2.3	1.3	1.2	1.1	0.4	0.4	0.3	0.3	0.1	0.1	0.1

[a]The values were recalculated to atomic percent from the data presented in ref 7.

3.2. ASR Ash Particles. As mentioned above, some of the particles, especially those in the samples collected during longer exposures, appeared brighter in BSE contrast in the SEM overview micrograph (Figure 3). Based on the EDS analysis, most of these particles were found to be rich in Fe, which is expected to originate from the ASR ash. Based on the overview micrographs and the performed EDS analysis, it is evident that BSE brightness can be used as an indicator to differentiate between the olivine bed material and particles originating from the ASR ash. Therefore, the difference in BSE contrast was thus used to quantify the amount of ASR ash particles, where both the ASR and the olivine fractions were counted in 4–5 representative SEM overviews for each collected sample, resulting in about 500 particles in total per sample. The relative number of ASR ash particles found in all the samples is summarized in Table 5. From the obtained results, it can be seen that after 1 day of exposure, the proportion of ASR ash particles is about 8%. This increases to about 40% after 4 days of exposure and remains unchanged in the later stages of the experiment, despite the further addition of ASR ash to the bed material. The noted lack of change in the relative percentage of ash particles may be attributed to the merging of smaller ash particles to form larger ash particles, as well as to the addition of fresh olivine, which was necessary to maintain the pressure drop needed for fluidization. A reduction of the number of ash particles could also arise from attrition, as they are most likely less-resistant to attrition than olivine. However, mechanical strength testing needs to be conducted to confirm this hypothesis.

To obtain statistical information about the ash particles, EDS-point analyses were recorded for 136 particles that were identified as ASR ash particles based on their bright BSE contrast. From the performed analyses, an average composition (O- and C-free basis) of these particles was calculated and is shown in Figure 9a. While the composition of each particle varies, Fe and Si are deemed to be the most-abundant elements. The high contents of Fe and Si agree with the composition of ASR ash derived from the total elemental analysis in Table 3. However, the specific composition of each ash particle varies significantly. This is exemplified by the Fe concentration, which is shown for all the particles in Figure 9b. It is clear that the concentration ranges from less than 1 at. % to 78 at. % Fe. Other major elements found in the ash particles are Ca, Al, and Zn. The average concentration of Mg in the pure ASR ash is lower than that observed on the ash particles, which could be a result of Mg diffusion from the olivine into the ash particles. The presence of K could be due to interactions with the biomass ash.

Based on the obtained compositions of the ASR ash particles, FactSage equilibrium calculations were conducted. The equilibrium composition was calculated separately for each EDS-point, due to the mentioned high-level variability of the compositions. The stable phases for each point were aggregated and are shown in Figure 10.

Figure 10a shows the thermodynamically stable phases under reducing conditions. The most-abundant phase is a mixed solid solution of metal oxides, consisting of mainly FeO, MgO, and ZnO. Slag formation is expected for particles that are rich in Si, and the slag phase consists of SiO_2, K_2O, Na_2O, and Al_2O_3. A solid solution of olivine is calculated to be composed of mixed $(Mg, Ca, Fe)_2SiO_4$, as well as clinopyroxene $[CaMg(Si_2O_6)]$, spinel $[(Mg, Fe, Zn)_3O_4]$, and melilite $[Ca_2(Zn, Mg)Si_2O_7]$. Furthermore, metallic Fe is calculated to be present in the particles that consist mostly of Fe.

Figure 10b shows the thermodynamically stable compositions under oxidizing conditions. The concentration of slag is expected to be higher under these conditions. $(Fe, Mg, Zn)O$ and olivine, which are the solid solutions that contain Fe^{2+} ions, are almost completely absent under these conditions, and the concentration of spinel (with Fe^{3+} ions) increases significantly.
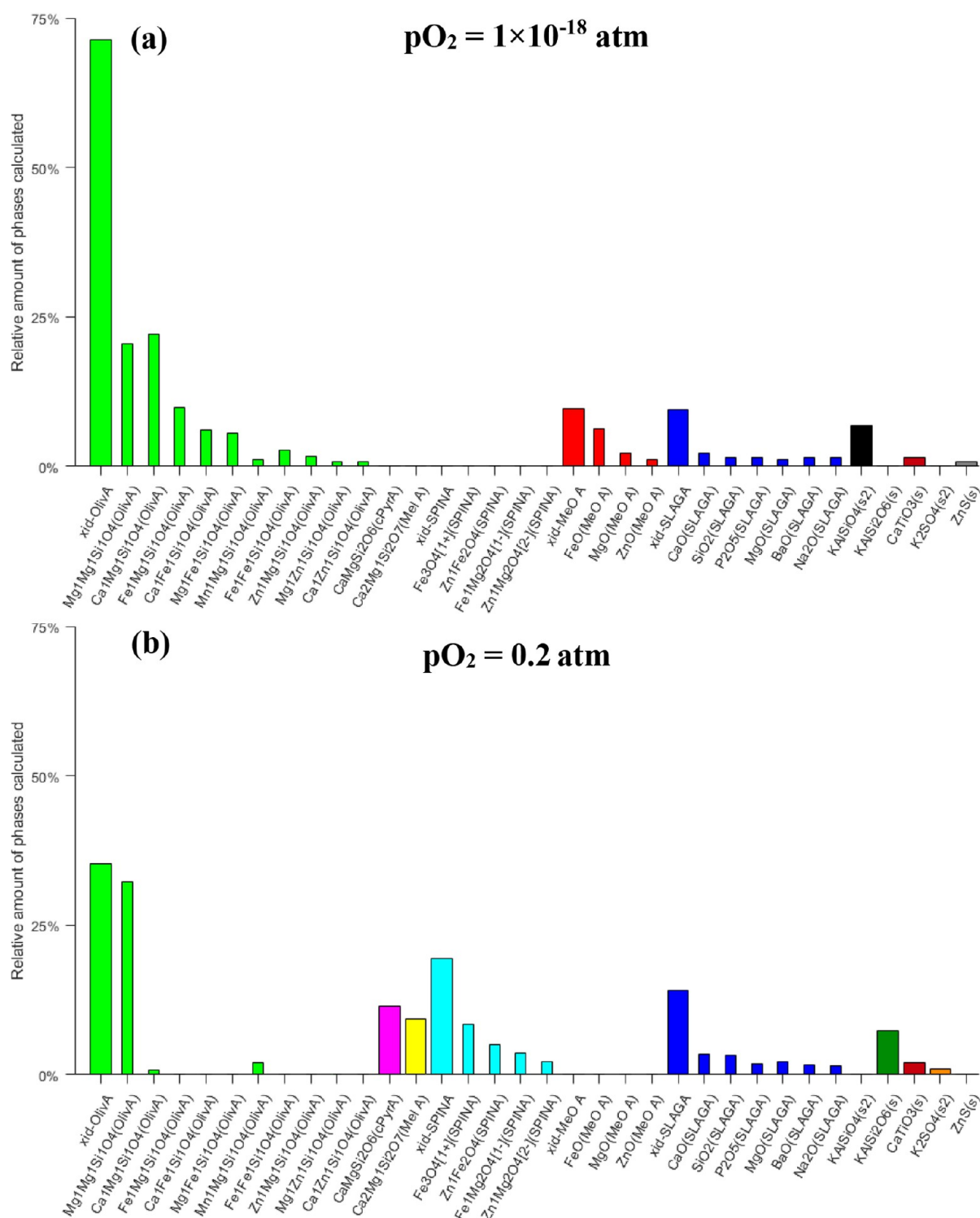
Figure 7. Phase composition of the bed material extracted after 13 days of feeding ASR to the gasifier, as derived from thermodynamic calculations with FactSage for conditions of 850 °C, 1 atm, and varying partial pressures of oxygen [reducing conditions (gasifier) and oxidizing conditions (combustor)].

Fe_2O_3 is calculated to form instead of Fe under oxidizing conditions, as a stable Fe-containing phase. A large fraction of the particles was calculated to contain Si-rich slag, thereby supporting the previously mentioned hypothesis related to the merging of ash particles.

Comparing the composition of the total bed material extracted after day 13 (Table 4) with the average composition

of the ash particles (Figure 9a), it is possible to estimate which elements are more likely to be found in the ash particles or the layered olivine. Assuming that 35% of the bed is made up of ash particles after 13 days (Table 5) that have the average composition indicated in Figure 9a, the concentrations of elements remaining in the layered olivine particles can be estimated using eq 1, in which $n_{i,olivine}$, $n_{i,total}$ and $n_{i,ASR}$ describe
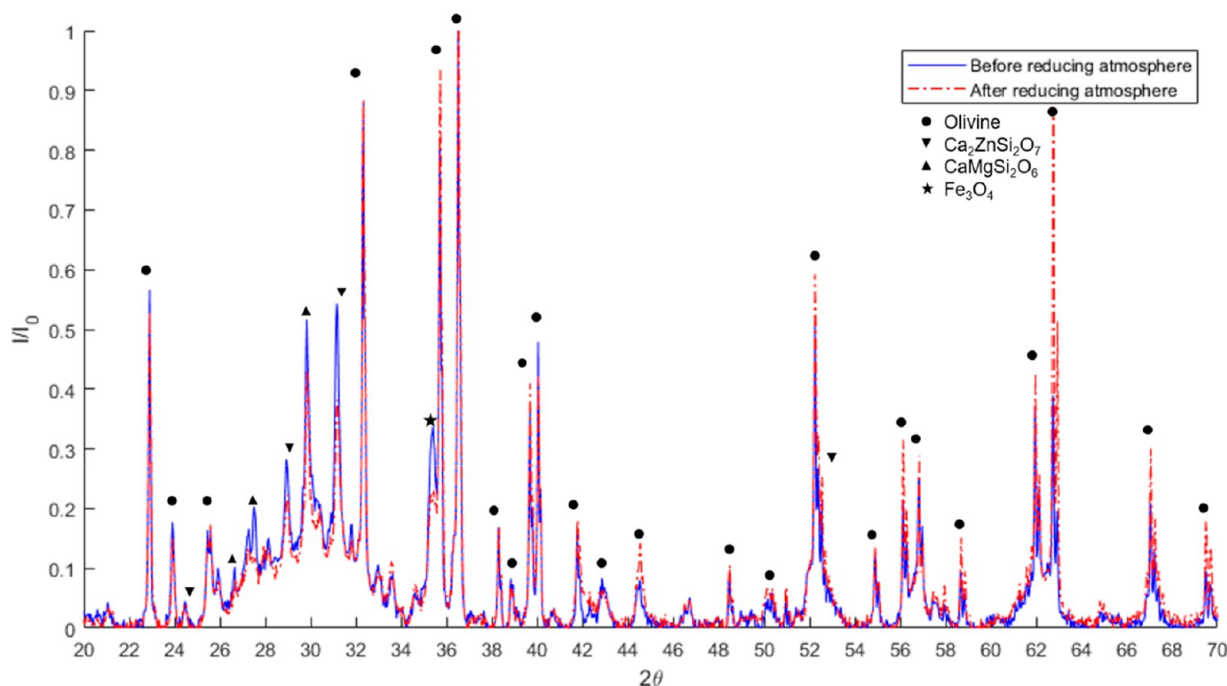
Figure 8. XRD results for the bed material particles extracted after 13 days of the experimental campaign before and after exposure for 40 s in a reducing atmosphere (50% CO with 50% N_2). The blue line indicates the data from the sample as-extracted, and the red line shows the data after reduction of the samples for 40 s in a fluidized bed batch reactor.

Table 5. Relative Amounts of ASR Ash Particles (Observed as Bright in Contrast Particles), as Determined in Overview SEM Scans of the Samples Exposed for Different Times to ASR

sample	relative amount of ASR ash particles
day 1	8%
day 4	40%
day 7	37%
day 13	35%

the concentration of each element in the olivine particles, the total ash composition, and the ash particles, respectively. The results are shown in Table 6. Note that some of the values are

negative, which is obviously impossible and indicates that a more-extensive analysis is necessary to increase the statistical accuracy of the data. Comparing $n_{i,ASR}$ with $n_{i,olivine}$, it can be seen that Ca, Al, K, Ti, Mn, Cu, Si, Cr, Na, Zn, and Fe are more likely to be found in the ash particles, whereas Mg, Si, P, Ba, and Ni are more abundant in the olivine. This trend can be utilized when recycling of trace metals (such as Cu and Zn) is attempted.[38,49]

$$n_{i,\text{olivine}} = \frac{n_{i,\text{total}} - n_{i,\text{ASR}} \times 0.35}{1 - 0.35} \quad (1)$$

Pissot et al.[7] have pointed out that the critical parameter for the CLG process to function is the oxygen-carrying ability of the bed material. Among the suggested bed compounds, those able
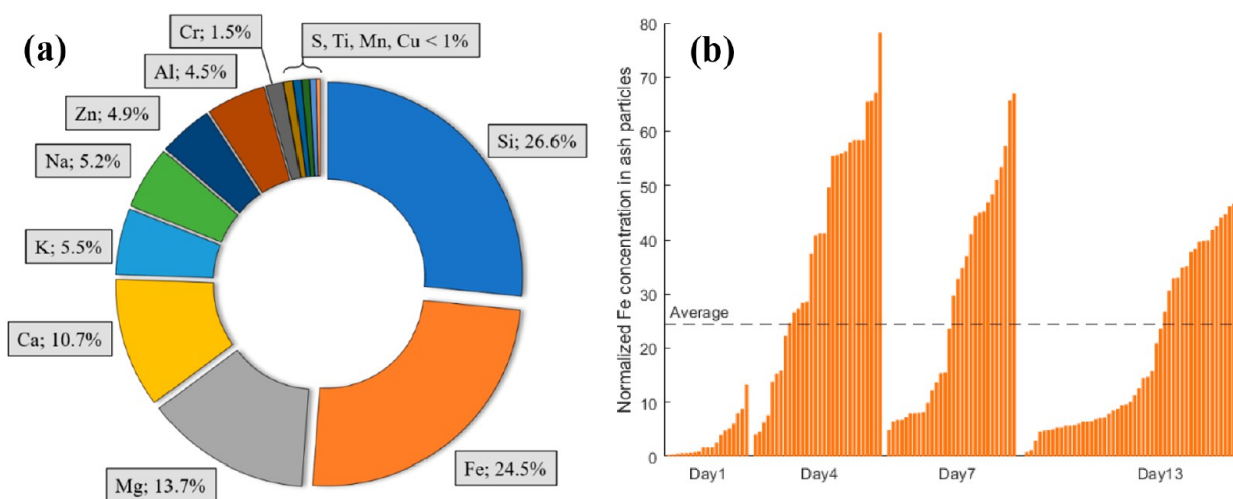

Figure 9. Average compositions (in at. %) obtained from 136 EDS-point analyses of all the particles identified as ASR ash particles (O- and C-free basis) (a) and the normalized concentrations of Fe in all the EDS-point analyses conducted on particles identified as ASR ash particles (b).
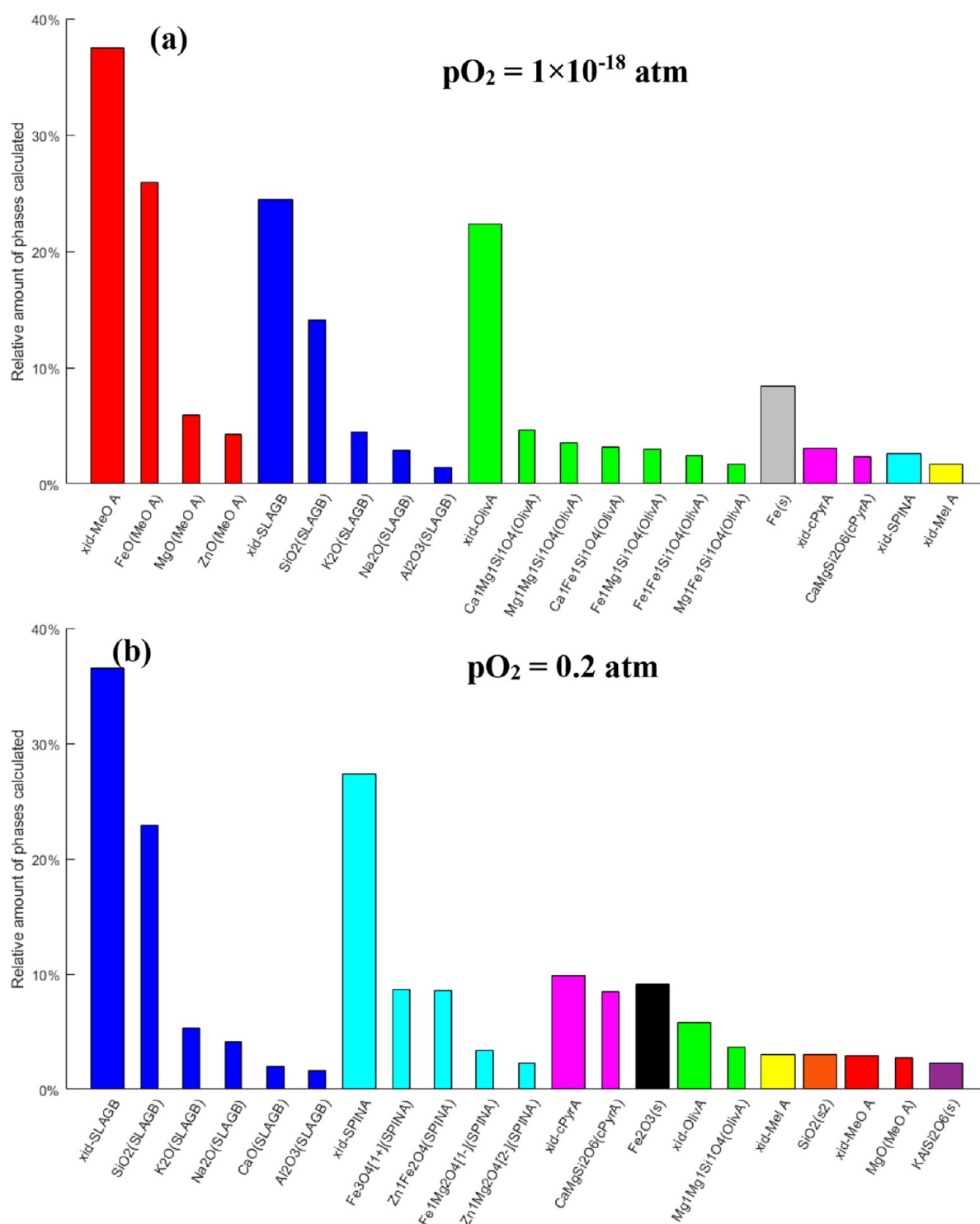
Figure 10. Phases calculated with the FactSage 7.2 software for the compositions of the particles with bright BSE contrast. The results are shown for (a) $pO_2 = 1 \times 10^{-18}$ atm and (b) $pO_2 = 0.2$ atm. The calculations were performed for conditions of 850 °C and 1 atm. Phases with an insignificant total amount have been omitted for clarity. The wide bars represent a solid solution that consists of the phases shown with narrow bars.

Table 6. Average Composition in Atomic Percent of Ash Particles (n_{ASR}) and Calculated Composition of Olivine Particles after 13 Days ($n_{olivine}$)[a]

	Mg	Si	Ca	Al	P	K	Ti	Mn	Cu	Ba	Ni	S	Cr	Na	Zn	Fe
n_{ASR}	13.7	26.6	10.7	4.5	0.3	5.5	0.6	0.6	0.5	n.d.	n.d.	0.8	1.4	5.2	4.9	24.5
$n_{olivine}$	52.5	37.5	8.5	2.4	1.7	0.6	0.3	0.3	0.2	0.2	0.2	0.1	<0	<0	<0	<0

[a]No Ba or Ni was detected in the ash particles (n.d.).

to participate in oxygen transport are Fe-enriched. According to the thermodynamic modeling results, alternation of Fe^{2+} under reducing conditions with Fe^{3+} under oxidizing conditions appears to be of the greatest importance regarding the activities of the ash particles. This alternation and the participation of Fe in oxygen transport are in agreement with the results reported by Pissot et al.[7]

A number of ash particles, at later stages of ASR addition, exhibit a hollow morphology in the SEM micrographs (see Figure 3d). The formation of hollow particles seems to be favored by longer exposure times, as their number and diameter increase until day 7 of the exposure. Table 7 shows the relative

Table 7. Relative Amount of Hollow Particles among the Counted Ash Particles as Well as their Average Diameter

	hollow particles among ash particles	diameter of hollow ash particles (μm)
day 1	0%	n.a.[a]
day 4	11%	160 ± 40
day 7	39%	270 ± 80
day 13	37%	290 ± 100

[a]n.a. = not applicable.

amount of hollow particles among the ash particles and their average diameter. An increase in diameter can be observed, which agrees with the previously mentioned merging of ash particles. This effect could be responsible for the lack of increase in the relative amount despite the further addition of ASR. Similar hollow particles have been noted previously[50,51] and have been attributed to local hotspots occurring in the vicinity of fuel particles during their conversion. Further analysis of two ash particles (a hollow one and a highly porous one) was performed to identify the differences in ash buildup. The results of the EDS-point analysis recorded for two particles extracted after 13 days of exposure to ASR ash are shown in Figure 11. Points 1, 2, and 3 were recorded in the upper particle, which represents a hollow particle. The recorded compositions were found to be similar, with 14−25 at. % of both Mg and Ca and around 35 at. % Si.

Together with K and Na (which were also detected), Si tends to form low-melting-point silicates. According to the thermodynamic equilibrium calculations, partial melt formation occurs in the three points recorded on the upper particle. As the formation of the hollow particles has been attributed to melt formation, the present observations are in agreement with those made in previous studies.[50,51] Furthermore, local hotspots may occur when ash-rich char is transported into the combustor, where the temperatures can be considerably higher in the vicinity of burning particles. Glass particles, which are present in ASR,[6] could be the source of the observed Si, Na, and Ca.

Bed material agglomeration was not reported as an issue during the campaign in which ASR was used as the fuel. However, a consequence of the interaction between an olivine particle and an ASR ash particle is depicted in Figure 11. EDS-point analysis was performed on the attached ash particle to evaluate the risk for agglomeration of the bed. Points 5 and 6 on the attached ash particle exhibited a composition similar to that of the previously discussed hollow particle, albeit with a lower Ca concentration. Instead, the concentration of K was higher, which is commonly attributed to agglomeration when found in combination with Si. Again, the FactSage calculations of the compositions at points 5 and 6 indicate partial melt formation at 850 °C. The composition of point 4 deviated from those at the other points, whereby 37% Fe and 13% Zn were detected. The concentrations of Si and Ca were significantly lower at point 4 than at the other points. A possible explanation for the local enrichment of elements that originate from the ASR ash is the incorporation of an ASR ash particle into a molten matrix.

3.3. Development of Oxygen-Carrying Ability. The oxygen-carrying effect of the bed material was measured as described previously by Pissot et al.[7] and Israelsson et al.[52] The measured oxygen transport as shown in Figure 12 is a combination of the oxygen-carrying ability (potential) of the particles and the contact between the fuel and particles in the reactor. The data are shown in Figure 12 and are presented as a ratio of the oxygen transferred by the bed material divided by the required oxygen for stoichiometric conversion of the fuel.
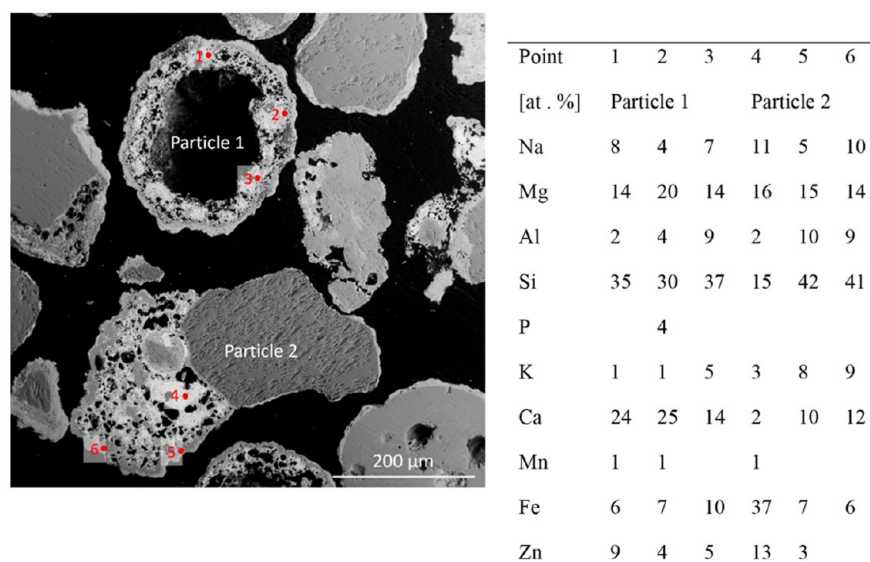

Point	1	2	3	4	5	6
[at . %]	Particle 1			Particle 2		
Na	8	4	7	11	5	10
Mg	14	20	14	16	15	14
Al	2	4	9	2	10	9
Si	35	30	37	15	42	41
P		4				
K	1	1	5	3	8	9
Ca	24	25	14	2	10	12
Mn	1	1		1		
Fe	6	7	10	37	7	6
Zn	9	4	5	13	3	

Figure 11. BSE micrograph (left) of a bed material sample extracted after 13 days of ASR addition. The micrograph shows a hollow particle (particle 1) and an ash particle which is attached to an olivine particle (particle 2). EDS-point analysis (right) was conducted, and the compositions corresponding to the points on the micrographs are shown in atomic percent (at. %) on an O- and C-free basis.
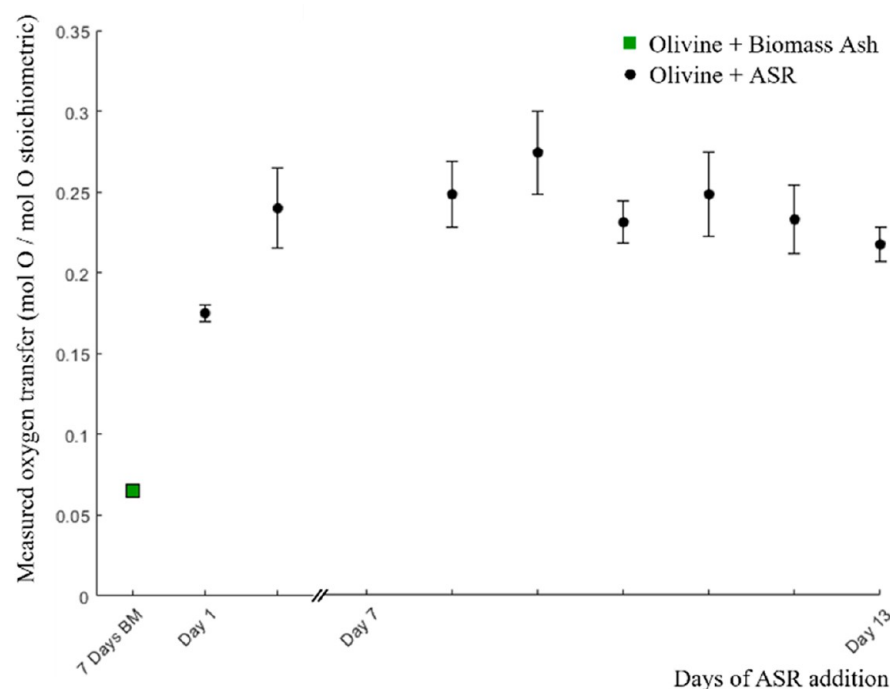
Figure 12. Measured oxygen transfer in moles of oxygen divided by the amount of oxygen required for the stoichiometric conversion of the fuel. For comparison, a value was added from Berdugo Vilches et al.[35] for the state of the olivine bed material after 7 days of biomass ash interaction, which is equivalent to the olivine at the beginning of ASR addition. Unfortunately, no data are available for days 3−7.
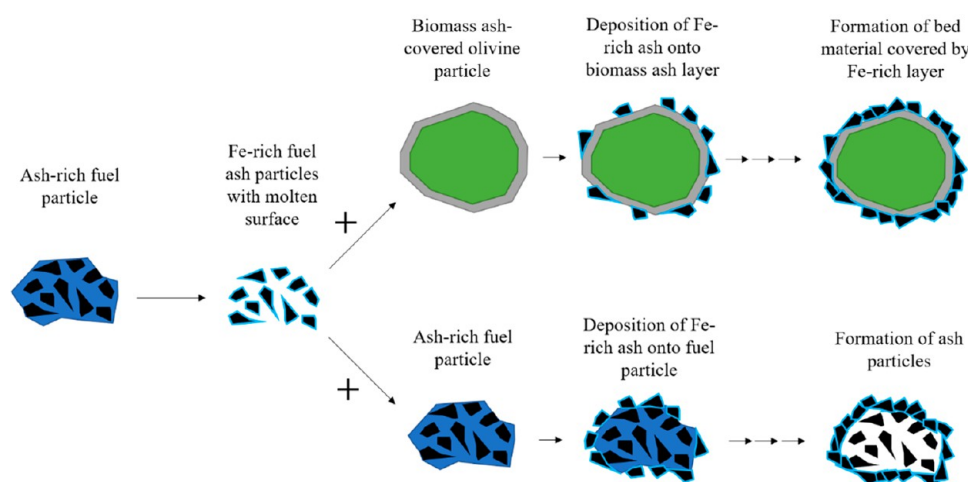

Figure 13. Schematic representation of the mechanism underlying the formation of the ASR ash-covered olivine particles and ASR ash particles.

Berdugo Vilches et al.[35] measured the oxygen carrying of olivine which had interacted with woody biomass ash for 7 days in the same reactor, which corresponds the state of the material at the beginning of the experimental campaign with ASR ash.

The oxygen transfer of the bed material increases rapidly within the first 2 days of ASR addition. This observation is in line with the fast increase in the relative amount of ash particles. After 1 day only 8% of the bed consisted of ash particles, compared to 40% after 4 days (see Table 5). Thermodynamic calculations concluded that a change in the oxidation state of Fe is responsible for the oxygen carrying (see Figure 10), and the majority of Fe was found to be in the ash particles (see Table 6). Thus, the share of ash particles in the bed material seems to be of major influence regarding the oxygen-carrying effect.

The continuation of ASR addition to the system does not increase the oxygen transport any further, as the values recorded

for day 2 and days 8−13 are similar, with a slight downward trend. This observation agrees with the decrease in ash particle concentration which likewise undergoes a slight downward trend (40% after 4 days, 37% after 7 days, and 35% after 13 days). While both decreasing trends could be caused by statistical fluctuations, an increased tendency for the formation of larger ash particles was observed. Larger ash particles provide less active surface area available for Fe^{2+}/Fe^{3+} cycles. However, further research is needed to confirm the extent of these trends.

The presence of Fe-rich particles enables applications of the used bed material in thermal conversion processes that require oxygen carriers, such as chemical looping combustion (CLC) or oxygen carrier-aided combustion (OCAC). Furthermore, the application of magnetic separation would concentrate the ASR ash particles into a single ash fraction. This fraction could then be used for recycling metals, or it might find application as an

oxygen carrier. Among the various Fe-bearing phases obtained through equilibrium calculations (Fe, FeO, olivine, hematite, and Fe-spinel), only Fe and Fe-spinel exhibit magnetic properties that could be exploited for separation at room temperature.[53−56] The formation of Fe-spinel was calculated to occur in significantly higher concentrations under oxidizing conditions than metallic Fe was calculated to form under reducing conditions. This suggests that if magnetic separation is utilized the particles can be extracted in their oxidized state, which means that extraction should be performed after the combustor. Alternatively, the formation of hollow ash particles could facilitate separation techniques that exploit the low density of these particles.

3.4. Mechanism. The mechanism by which both ash-covered olivine particles and ASR ash particles are formed is shown schematically in Figure 13. The organic fraction of the ash-rich fuel particle is converted to gas, which then leaves the reactor. The remaining inorganic fraction is partially molten at the temperature in the gasifier, which facilitates the attachment of ash particles to other particles in the gasifier. These can be olivine particles, such that the continuous accumulation of small ash particles leads to the formation of an Fe-rich layer. Alternatively, the smaller ash particles can attach to other unconverted fuel particles, which can then collect additional particles to form larger agglomerates of fuel ash particles.

4. CONCLUSION

Olivine particles utilized as the bed material for indirect gasification were analyzed regarding their interactions with ASR and biomass ash. SEM analysis revealed the formation of Fe-rich layers on the olivine particles, and these are likely to contribute to the oxygen transport capability of the olivine. A low level of agglomeration of the ash and olivine particles was observed for longer exposure times.

About one-third of the bed consisted of ash particles that were rich in Fe and Si. FactSage calculations of these particles under oxidizing and reducing conditions indicate alternation between Fe^{2+} and Fe^{3+} as the main contribution to oxygen carriage. Metallic iron formation was calculated under reducing conditions for particles that primarily were comprised of Fe. The separation of particles rich in ASR ash elements into a single ash fraction might enable metal recycling from the ASR ash. Even though the overall oxygen-carrying capability of the inventory increases, a selective separation and extraction step for either the Fe-rich or Fe-lean fraction would allow stringent control of the conditions. The presence of Fe-spinel under oxidizing conditions suggests that the particles leaving the combustor have magnetic properties.

Lastly, the high concentration of Fe in the bed material could enable further applications in fluidized bed thermal conversion processes for which oxygen-carrying bed materials are required, such as CLC and OCAC.

AUTHOR INFORMATION

Corresponding Author

Robin Faust − *Department of Chemistry and Chemical Engineering, Chalmers University of Technology, SE-41296 Göteborg, Sweden;* orcid.org/0000-0001-5614-3578; Email: faust@chalmers.se

Authors

Panida Aonsamang − *Department of Chemistry and Chemical Engineering, Chalmers University of Technology, SE-41296 Göteborg, Sweden*

Jelena Maric − *Akademiska Hus Chalmers Kraftcentralen, 412 96 Göteborg, Sweden;* orcid.org/0000-0002-8885-1648

Alyona Tormachen − *Department of Chemistry and Chemical Engineering, Chalmers University of Technology, SE-41296 Göteborg, Sweden*

Martin Seemann − *Division of Energy Technology, Department of Space, Earth, and Environment, Chalmers University of Technology, 412 96 Göteborg, Sweden*

Pavleta Knutsson − *Department of Chemistry and Chemical Engineering, Chalmers University of Technology, SE-41296 Göteborg, Sweden*

Complete contact information is available at:
https://pubs.acs.org/10.1021/acs.energyfuels.1c02137

Notes
The authors declare no competing financial interest.

REFERENCES

(1) Mehlhart, G.; Kosińska, I.; Baron, Y.; Hermann, A. *Assessment of the implementation of the ELV Directive with emphasis on the end of life vehicles of unknown whereabouts*; European Commission, 2017.
(2) European Parliament and Council.. Directive 2000/53/EC on end-of-life vehicles. *Off. J. Eur. Union* **2000**, *L269*, 34−42.
(3) Williams, K. S.; Khodier, A. Meeting EU ELV targets: Pilot-scale pyrolysis automotive shredder residue investigation of PAHs, PCBs and environmental contaminants in the solid residue products. *Waste Manage.* **2020**, *105*, 233−239.
(4) Groke, M.; Kaerger, W. Optimierung der Separation von Bauteilen und Materialien aus Altfahrzeugen zur Rückgewinnung kritischer Metalle (ORKAM). *UBA Texte* **2017**, *02*.
(5) Vermeulen, I.; Van Caneghem, J.; Block, C.; Baeyens, J.; Vandecasteele, C. Automotive shredder residue (ASR): Reviewing its production from end-of-life vehicles (ELVs) and its recycling, energy or chemicals' valorisation. *J. Hazard. Mater.* **2011**, *190* (1−3), 8−27.
(6) Morselli, L.; Santini, A.; Passarini, F.; Vassura, I. Automotive shredder residue (ASR) characterization for a valuable management. *Waste Manage.* **2010**, *30* (11), 2228−2234.
(7) Pissot, S.; Berdugo Vilches, T.; Maric, J.; Cañete Vela, I.; Thunman, H.; Seemann, M. Thermochemical Recycling of Automotive Shredder Residue by Chemical-Looping Gasification Using the Generated Ash as Oxygen Carrier. *Energy Fuels* **2019**, *33*, 11552.
(8) Harder, M. K.; Forton, O. T. A critical review of developments in the pyrolysis of automotive shredder residue. *J. Anal. Appl. Pyrolysis* **2007**, *79*, 387−394.
(9) Lundqvist, U.; et al. Design for Recycling in the Transport Sector-Future Scenarios and Challenges. *CPM Rep.* **2004**, *2004*, 7.
(10) Buekens, A.; Zhou, X. Recycling plastics from automotive shredder residues: A review. *J. Mater. Cycles Waste Manage.* **2014**, *16* (3), 398−414.

(11) Emilsson, E.; Dahllöf, L.; Söderman, M. L. Plastics in passenger cars: A comparison over types and time. *IVL Swedish Environ. Res. Inst.* **2019**, November.

(12) Merkisz-Guranowska, A. Waste recovery of end-of-life vehicles. *IOP Conf. Ser.: Mater. Sci. Eng.* **2018**, *421* (3), 032019.

(13) European Commision. *On the Implementation of Directive 2000/53/Ec on End-of-Life Vehicles* **2017**.

(14) Kanari, N.; Pineau, J. L.; Shallari, S. End-of-Life Vehicle Recycling in the European Union. *JOM* **2003**, *55* (8), 15−19.

(15) Cossu, R.; Lai, T. Automotive shredder residue (ASR) management: An overview. *Waste Manage.* **2015**, *45*, 143−151.

(16) Vermeulen, I.; Block, C.; Van Caneghem, J.; Dewulf, W.; Sikdar, S. K.; Vandecasteele, C. Sustainability assessment of industrial waste treatment processes: The case of automotive shredder residue. *Resour. Conserv. Recycl.* **2012**, *69*, 17−28.

(17) Cossu, R.; Lai, T. Washing treatment of automotive shredder residue (ASR). *Waste Manage.* **2013**, *33* (8), 1770−1775.

(18) Commission of the European Communities.. *Commission of the European Communities Report from the Commission to the Council and the European Parliament on the targets contained in article 7(2)(b) of Directive 2000/53/EC on End-of-Life Vehicle—Impact Assessment* **2007**, *7*, 142.

(19) Haydary, J.; Susa, D.; Gelinger, V.; Čacho, F. Pyrolysis of automobile shredder residue in a laboratory scale screw type reactor. *J. Environ. Chem. Eng.* **2016**, *4* (1), 965−972.

(20) Yang, B.; Chen, M. Influence of interactions among polymeric components of automobile shredder residue on the pyrolysis temperature and characterization of pyrolytic products. *Polymers (Basel, Switz.)* **2020**, *12* (8), 1682.

(21) Maric, J.; Berdugo Vilches, T.; Pissot, S.; Cañete Vela, I.; Gyllenhammar, M.; Seemann, M. Emissions of dioxins and furans during steam gasification of Automotive Shredder residue; experiences from the Chalmers 2−4-MW indirect gasifier. *Waste Manage.* **2020**, *102*, 114−121.

(22) Roh, S. A.; Kim, W. H.; Yun, J. H.; Min, T. J.; Kwak, Y. H.; Seo, Y. C. Pyrolysis and gasification-melting of automobile shredder residue. *J. Air Waste Manage. Assoc.* **2013**, *63* (10), 1137−1147.

(23) Zhao, H.; Wang, J. Chemical-looping combustion of plastic wastes for in situ inhibition of dioxins. *Combust. Flame* **2018**, *191*, 9−18.

(24) Lopes, E. J.; Okamura, L. A.; Yamamoto, C. I. Formation of dioxins and furans during municipal solid waste gasification. *Braz. J. Chem. Eng.* **2015**, *32* (1), 87−97.

(25) Fürsatz, K.; Fuchs, J.; Benedikt, F.; Kuba, M.; Hofbauer, H. Effect of biomass fuel ash and bed material on the product gas composition in DFB steam gasification. *Energy* **2021**, *219*, 119650.

(26) Faust, R.; Berdugo Vilches, T.; Malmberg, P.; Seemann, M.; Knutsson, P. Comparison of Ash Layer Formation Mechanisms on Si-Containing Bed Material during Dual Fluidized Bed Gasification of Woody Biomass. *Energy Fuels* **2020**, *34* (7), 8340−8352.

(27) Wagner, K.; Haggstrom, G.; Mauerhofer, A. M.; Kuba, M.; Skoglund, N.; Ohman, M.; Hofbauer, H.; et al. Layer formation on K-feldspar in fluidized bed combustion and gasification of bark and chicken manure. *Biomass Bioenergy* **2019**, *127*, 105251.

(28) Hannl, T. K.; Faust, R.; Kuba, M.; Knutsson, P.; Berdugo Vilches, T.; Seemann, M.; Ohman, M.; et al. Layer Formation on Feldspar Bed Particles during Indirect Gasification of Wood. 2. Na-Feldspar. *Energy Fuels* **2019**, *33* (8), 7333−7346.

(29) Faust, R.; Hannl, T. K.; Vilches, T. B.; Kuba, M.; Ohman, M.; Seemann, M.; Knutsson, P. Layer Formation on Feldspar Bed Particles during Indirect Gasification of Wood. 1. K-Feldspar. *Energy Fuels* **2019**, *33*, 7321.

(30) Wagner, K.; Haggstrom, G.; Skoglund, N.; Priscak, J.; Kuba, M.; Ohman, M.; Hofbauer, H.; et al. Layer formation mechanism of K-feldspar in bubbling fluidized bed combustion of phosphorus-lean and phosphorus-rich residual biomass. *Appl. Energy* **2019**, *248*, 545−554.

(31) Kuba, M.; et al. Mechanism of layer formation on olivine bed particles in industrial-scale dual fluid bed gasification of wood. *Energy Fuels* **2016**, *30* (9), 7410−7418.

(32) He, H.; Skoglund, N.; Öhman, M. Time-Dependent Layer Formation on K-Feldspar Bed Particles during Fluidized Bed Combustion of Woody Fuels. *Energy Fuels* **2017**, *31* (11), 12848−12856.

(33) He, H.; Ji, X.; Boström, D.; Backman, R.; Öhman, M. Mechanism of Quartz Bed Particle Layer Formation in Fluidized Bed Combustion of Wood-Derived Fuels. *Energy Fuels* **2016**, *30* (3), 2227−2232.

(34) Grimm, A.; Skoglund, N.; Boström, D.; Öhman, M. Bed agglomeration characteristics in fluidized quartz bed combustion of phosphorus-rich biomass fuels. *Energy Fuels* **2011**, *25* (3), 937−947.

(35) Berdugo Vilches, T.; Marinkovic, J.; Seemann, M.; Thunman, H. Comparing Active Bed Materials in a Dual Fluidized Bed Biomass Gasifier: Olivine, Bauxite, Quartz-Sand, and Ilmenite. *Energy Fuels* **2016**, *30* (6), 4848−4857.

(36) Maric, J.; Berdugo Vilches, T.; Thunman, H.; Gyllenhammar, M.; Seemann, M. Valorization of Automobile Shredder Residue Using Indirect Gasification. *Energy Fuels* **2018**, *32* (12), 12795−12804.

(37) Lyngfelt, A. Chemical Looping Combustion: Status and Development Challenges. *Energy Fuels* **2020**, *34* (8), 9077−9093.

(38) Staničić, I.; Cañete Vela, I.; Backman, R.; Maric, J.; Cao, Y.; Mattisson, T. Fate of lead, copper, zinc and antimony during chemical looping gasification of automotive shredder residue. *Fuel* **2021**, *302*, 121147.

(39) Larsson, A.; Seemann, M.; Neves, D.; Thunman, H. Evaluation of performance of industrial-scale dual fluidized bed gasifiers using the chalmers 2−4-MWth gasifier. *Energy Fuels* **2013**, *27* (11), 6665−6680.

(40) Leion, H.; Frick, V.; Hildor, F. Experimental Method and Setup for Laboratory Fluidized Bed Reactor Testing. *Energies* **2018**, *11*, 2505.

(41) Bale, C.W.; Chartrand, P.; Degterov, S.A.; Eriksson, G.; Hack, K.; Ben Mahfoud, R.; Melancon, J.; Pelton, A.D.; Petersen, S. FactSage thermochemical software and databases. *CALPHAD: Comput. Coupling Phase Diagrams Thermochem.* **2002**, *26* (2), 189−228.

(42) Faust, R.; Sattari, M.; Maric, J.; Seemann, M.; Knutsson, P. Microscopic investigation of layer growth during olivine bed material aging during indirect gasification of biomass. *Fuel* **2020**, *266*, 117076.

(43) Marinkovic, J.; Thunman, H.; Knutsson, P.; Seemann, M. Characteristics of olivine as a bed material in an indirect biomass gasifier. *Chem. Eng. J.* **2015**, *279*, 555−566.

(44) Berdugo Vilches, T.; Maric, J.; Knutsson, P.; Rosenfeld, D. C.; Thunman, H.; Seemann, M. Bed material as a catalyst for char gasification: The case of ash-coated olivine activated by K and S addition. *Fuel* **2018**, *224*, 85−93.

(45) Kirnbauer, F.; Hofbauer, H. Investigations on bed material changes in a dual fluidized bed steam gasification plant in Güssing, Austria. *Energy Fuels* **2011**, *25* (8), 3793−3798.

(46) Grimm, A.; Öhman, M.; Lindberg, T.; Fredriksson, A.; Boström, D. Bed agglomeration characteristics in fluidized-bed combustion of biomass fuels using olivine as bed material. *Energy Fuels* **2012**, *26* (7), 4550−4559.

(47) De Geyter, S.; Öhman, M.; Boström, D.; Eriksson, M.; Nordin, A. Effects of non-quartz minerals in natural bed sand on agglomeration characteristics during fluidized bed combustion of biomass fuels. *Energy Fuels* **2007**, *21* (5), 2663−2668.

(48) Devi, L.; Craje, M.; Thüne, P.; Ptasinski, K. J.; Janssen, F. J. J. G. Olivine as tar removal catalyst for biomass gasifiers: Catalyst characterization. *Appl. Catal. A Gen.* **2005**, *294* (1), 68−79.

(49) Staničić, I. *Fate of Trace Elements in Thermochemical Conversion of Waste Fuels Using Oxygen Carriers*. Thesis, Chalmers University of Technology, Gothenburg, Sweden, 2021.

(50) Gyllén, A.; Knutsson, P.; Lind, F.; Thunman, H. Magnetic separation of ilmenite used as oxygen carrier during combustion of biomass and the effect of ash layer buildup on its activity and mechanical strength. *Fuel* **2020**, *269*, 117470.

(51) Hanning, M.; Corcoran, A.; Lind, F.; Rydén, M. Biomass ash interactions with a manganese ore used as oxygen-carrying bed material in a 12 MWth CFB boiler. *Biomass Bioenergy* **2018**, *119*, 179−190.

(52) Israelsson, M.; Larsson, A.; Thunman, H. Online measurement of elemental yields, oxygen transport, condensable compounds, and

heating values in gasification systems. *Energy Fuels* **2014**, *28* (9), 5892–5901.

(53) Pichon, B. P.; Gerber, O.; Lefevre, C.; Florea, I.; Fleutot, S.; Baaziz, W.; Pauly, M.; Ohlmann, M.; Ulhaq, C.; Ersen, O.; Pierron-Bohnes, V.; Panissod, P.; Drillon, M.; Begin-Colin, S.; et al. Microstructural and magnetic investigations of Wüstite-spinel core-shell cubic-shaped nanoparticles. *Chem. Mater.* **2011**, *23* (11), 2886–2900.

(54) Dachs, E.; Geiger, C. A.; von Seckendorff, V.; Grodzicki, M. A low-temperature calorimetric study of synthetic (forsterite + fayalite) {(Mg2SiO4 + Fe2SiO4)} solid solutions: An analysis of vibrational, magnetic, and electronic contributions to the molar heat capacity and entropy of mixing. *J. Chem. Thermodyn.* **2007**, *39* (6), 906–933.

(55) Lu, H. M.; Meng, X. K. Morin Temperature and Neel Temperature of Hematite Nanocrystals. *J. Phys. Chem. C* **2010**, *114* (49), 21291–21295.

(56) Kozlenko, D. P.; Dubrovinsky, L. S.; Kichanov, S. E.; Lukin, E. V.; Cerantola, V.; Chumakov, A. I.; Savenko, B. N.; et al. Magnetic and electronic properties of magnetite across the high pressure anomaly. *Sci. Rep.* **2019**, *9* (1), 1–9.